Conformational changes in Dnm1 support a contractile mechanism for mitochondrial fission

Jason A. Mears, Laura L. Lackner, Shunming Fang, Elena Ingerman, Jodi Nunnari and Jenny E. Hinshaw

Supplementary Figures and Information

Nature Structural & Molecular Biology: doi:10.1038/nsmb.1949

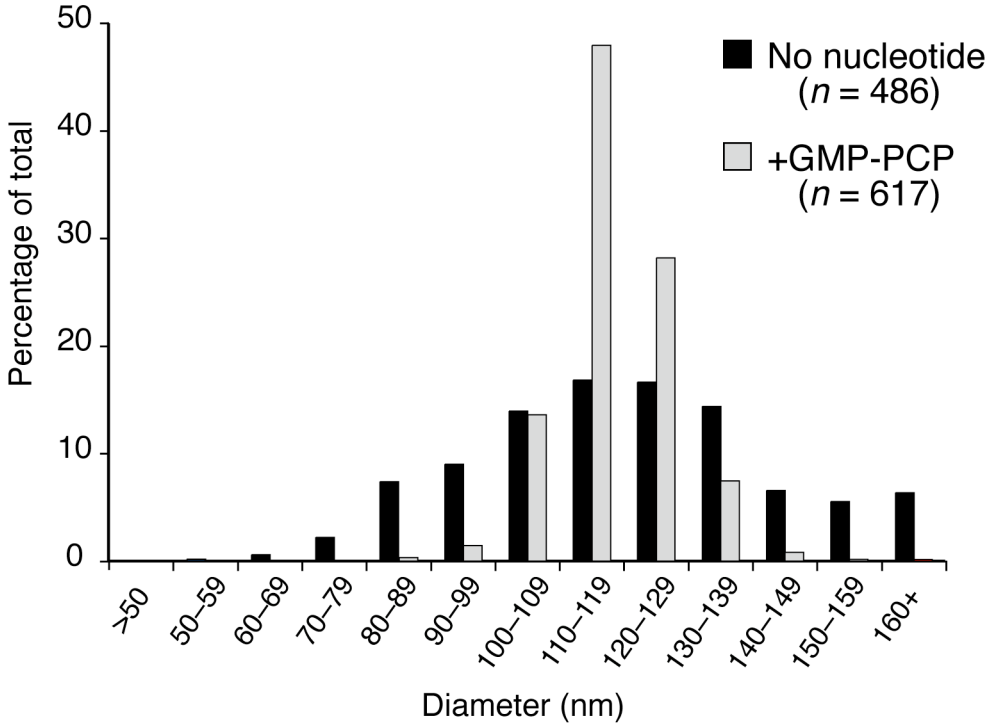

Supplementary Figure 1 Distribution of Dnm1 tube diameters. Histograms compare the corresponding helical diameters of Dnm1 tubes without nucleotide (apo, black) and with 1 mM GMP-PCP (GTP-bound, grey). Average diameter is 121 ± 25 nm in the apo state and 118 ± 9 nm in the GTP-bound state.

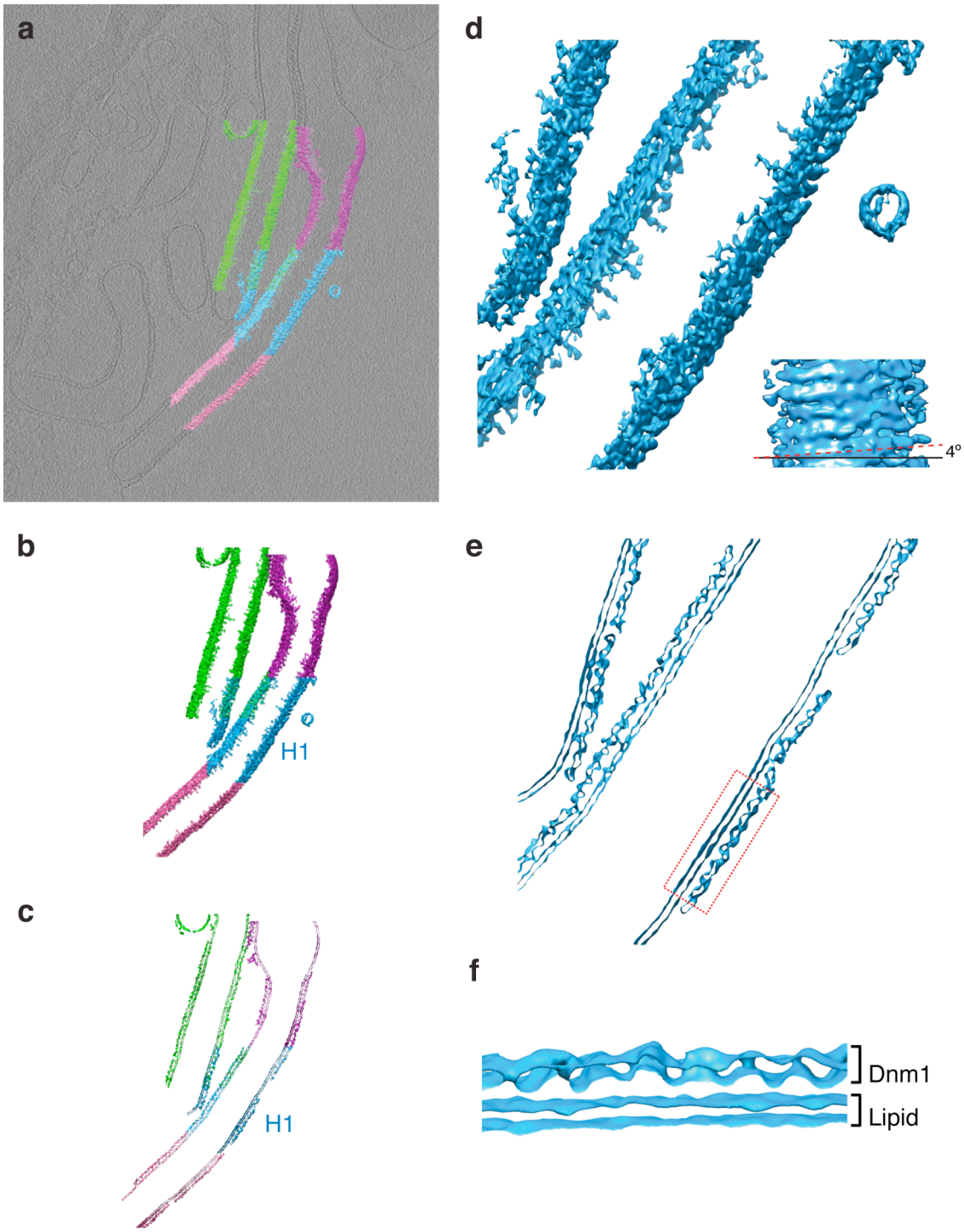

Supplementary Figure 2 Cryo-ET of Dnm1 helices. (**a** & **b**) Segmented Dnm1 helices are presented with a z-slice of the tomographic reconstruction (**a)** and alone (**b**). (**c**) A central section of the segmented tubes. (**d**) The segmented Dnm1 tube labeled H1 in **b**. A surface view illustrates the right-handedness of the Dnm1 helix with a 4º incline (lower right). (**e**) A central section of the H1 Dnm1 helix shown in **d** is presented. The red dashed box highlights the region shown in panel **f**. (**f**) A segment of the section presented in **e** illustrates the gap between the Dnm1 and lipid densities.

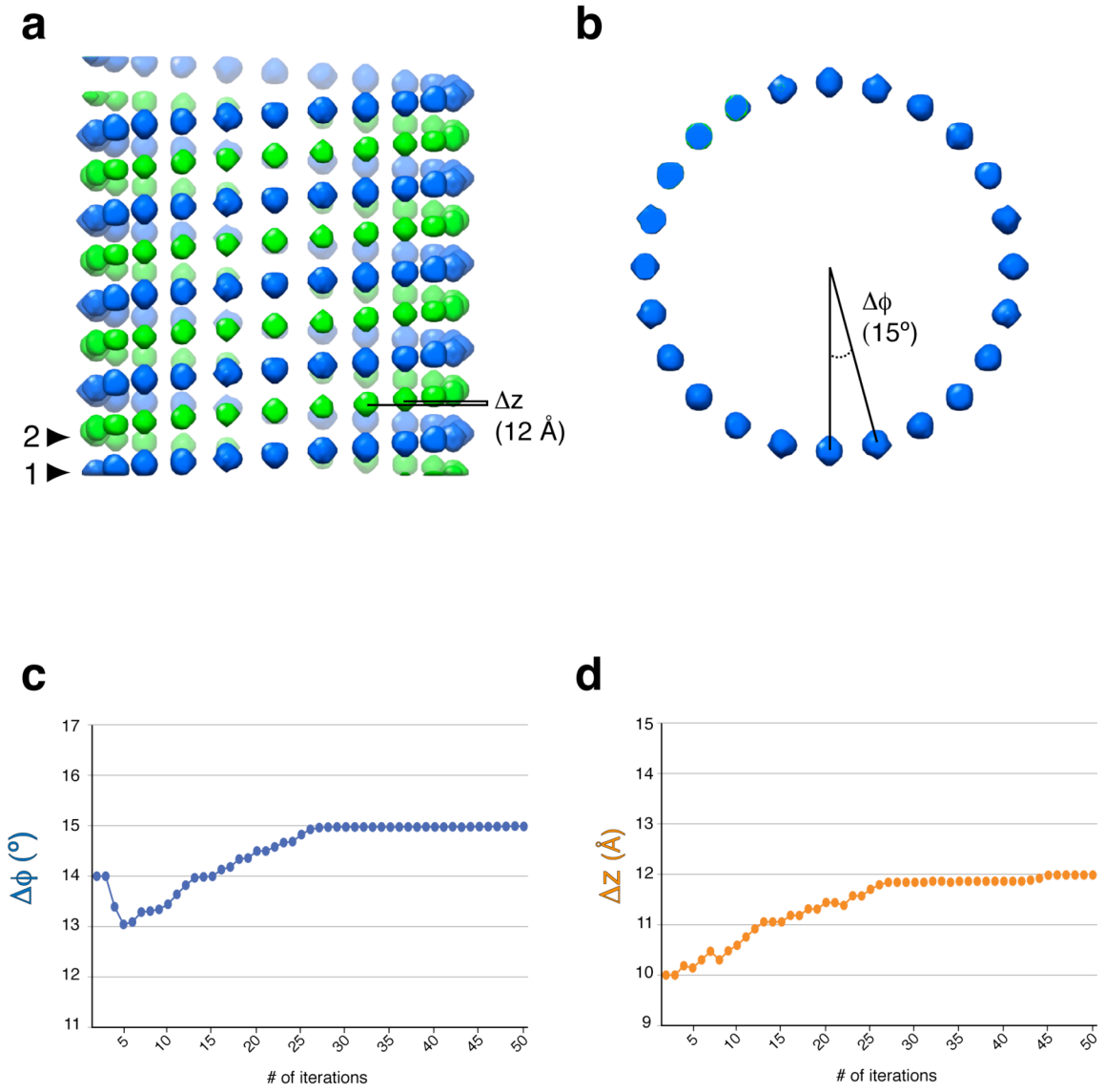

Supplementary Figure 3 3D reconstruction of Dnm1 tubes. (**a** & **b)** A representative model is presented with the helical parameters determined for the final 3D map of the Dnm1 helix. The z (rise per subunit) and ϕ (rotation per subunit) are highlighted. The two strands of the 2-start helix (offset by 14.4 nm and both with a 28.8 nm pitch) are colored blue and green. (**c** & **d**) The iterative search for the helical parameters of the Dnm1 helix merged after 50 cycles to 15.0º for ϕ and 12.0 Å for z.

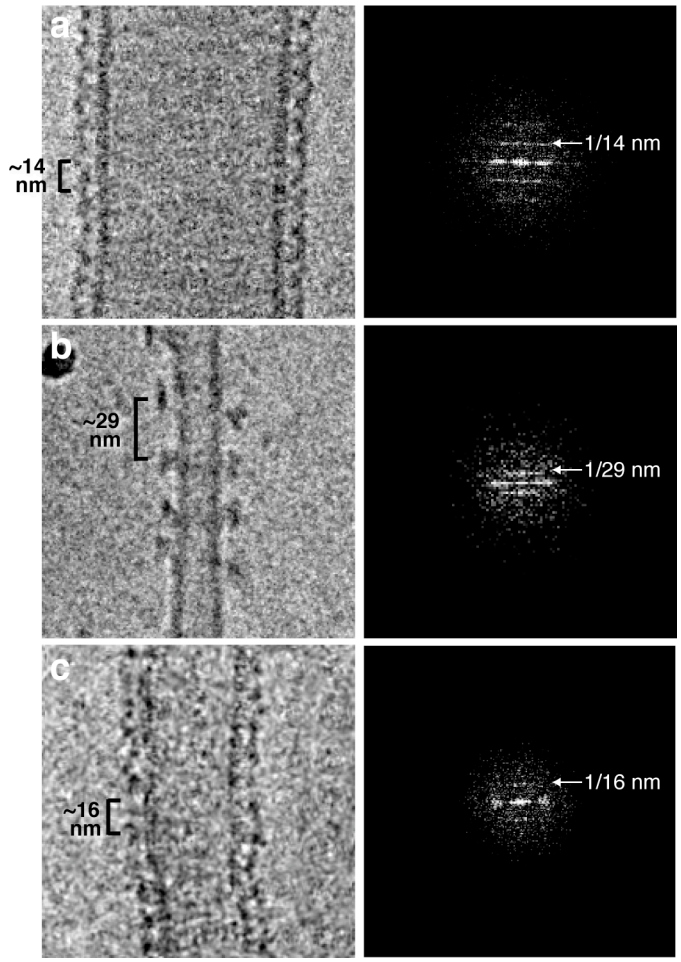

Supplementary Figure 4 Helical spacing of GTP-treated Dnm1-lipid tubes. (**a**) A representative Dnm1 tube (~105 nm diameter) observed after incubation with 1 mM GMP-PCP. The corresponding power spectrum (right panel) shows that the helical spacing measures ~14 nm. (**b**) A representative tube (~45 nm diameter) observed after addition of 1 mM GTP with the corresponding power spectrum that shows the helical spacing measures ~29 nm. (**c**) A representative tube observed after addition of 0.1 mM GTP (~55 nm diameter) and the corresponding power spectrum that measures the helical spacing at ~16 nm.

SUPPLEMENTARY METHODS

Single-particle helical reconstruction. As described in the methods, projection matching was used to sort 4,323 boxed segments based on tube diameter. Initially, segments were classified by diameter into datasets that varied by 5 nm from 95 nm to >140 nm. The most populous data sets had diameters of 110 nm (number of segments (n) = 607), 115 nm (n = 803), 120 nm (n = 771), 125 nm (n = 881) and 130 nm (n = 661). These data sets were used to reconstruct five 3D structure of Dnm1 using the IHRSR algorithm.

All 5 data sets resolved to 2-start helical symmetries, and all had a gap between the protein and underlying membrane. Despite having fewer particles in the dataset, the 130 nm stack and subsequent 3D structure were deemed to be better based on resolution and cross-correlation of the raw data to the final map. Also, the underlying membrane was more uniform (i.e. less rippled) with the 130 nm dataset, which implies that the alignment of the particles was better. The maps with the smaller diameters also had more noise in the final reconstruction despite having a comparable number of particles, which suggests that the alignment was less accurate.

Following from this work, we classified the boxed segments by diameter into groups that differ by only 1 nm. Again, the most abundant classes were the 115-130 nm diameters. A few of the individual classes were combined to get a number of particles sufficient for a clean reconstruction. We tested several combinations including 127-130 nm classes (n = 637), 127-131 nm classes (n = 710) and 128-131 nm classes (n = 586). In the end, the best structure was achieved using the 128-131 nm dataset based on the overall resolution and the cross-correlation of the raw images to the final reconstruction. The overall symmetry was determined to have 24 subunits per turn (ϕ = 15º) and a pitch of 28.8 nm (z = 12 Å).

In addition, we tested several starting helical parameters, and a majority merged to the helical parameters corresponding to 24 subunits per turn (ϕ = 15º) and a pitch of ~288 Å (z = 12 Å). Starting rotation angles of 12.8º (28 subunits/turn), 13.8º (26 subunits/turn), 15.0º (24 subunits/turn), and 15.6º (23 subunits/turn) merged to 15º (24 subunits/turn). Additionally, we examined larger starting rotation angles and one iteration (16.4º, or 22 subunits/turn) merged to ϕ = 17º, which would correspond to ~21 subunits per turn. The map is very similar to the ϕ = 15º solution, and the gap still exists between the protein and lipid. We also tested out-of-plane tilt correction with starting rotation angles of 13.8º and 16.4º, which merged to 15º and 17º respectively. In both cases, the pitch resolves to 28 nm. In the end, we chose to present the map with 24 subunits per turn (15º rotation angle) because it represents the majority of solutions determined using the IHRSR method.

To further confirm the 2-start structure, three new starting models were developed: 1) a 1-start helix with 24 subunits per turn and a helical pitch of 14 nm, 2) a 1-start helix with 24 subunits per turn and a helical pitch of 28 nm, and 3) a 2-start helix with 24 subunits per turn and a helical pitch of 28 nm (i.e. the same parameters found for the final map, Supplemental Fig. 3, **a** and **b**). Both models #2 and #3 resolved to a final structure nearly identical to the final 3D map, 2-start and 24 subunits per turn. When the 1-start model with a pitch of 14 nm (model #1) was used as a starting model for the iterative search, the helical parameters did not merge after 100 cycles, indicating that model #1 was far from accurate. Additionally, the particles in the dataset were cross-correlated to the final maps and the CC efficiency was ~30 to 40% better with the 2-start structure. Additionally, we cross-correlated the boxed helical segments against ideal 1-start (both 14 nm and 28 nm pitch) and 2-start projections in both real-space and Fourier-space. All of the segments correlated better with the ideal 2-start projections.

3D rendering of cryo-ET reconstruction. The final tomogram was presented in figure S2 using Chimera. The map was filtered using a 3D isotropic Gaussian function to a width of 7.8 (~5 nm), and the Hide Dust function was used to remove small particles based on a volume cutoff of ~25 nm^3.

Nature Structural & Molecular Biology: doi:10.1038/nsmb.1949